

AperTO - Archivio Istituzionale Open Access dell'Università di Torino

Synthesis, characterization and photocatalytic performance of p-type carbon nitride

This is the author's manuscript

Original Citation:

Availability:

This version is available <http://hdl.handle.net/2318/1689460> since 2019-02-04T12:54:02Z

Published version:

DOI:10.1016/j.apcatb.2018.09.057

Terms of use:

Open Access

Anyone can freely access the full text of works made available as "Open Access". Works made available under a Creative Commons license can be used according to the terms and conditions of said license. Use of all other works requires consent of the right holder (author or publisher) if not exempted from copyright protection by the applicable law.

(Article begins on next page)

Synthesis, characterization and photocatalytic performances of p-type Carbon Nitride

Gabriele Capilli, Mattia Costamagna, Fabrizio Sordello, Claudio Minero *

Dipartimento di Chimica, Università degli Studi di Torino – via Pietro Giuria 5 -10125 Torino, Italy

ABSTRACT

p-Type organic semiconductors are attractive to develop new photo- and photoelectro-catalytic systems, particularly if the conduction band is located at negative redox potentials. An easy synthetic route to produce carbon-doped carbon nitride ($C_{n>3}N_4$) with a stable p-type semiconducting character was optimized. The precursors used were melamine and triaminopyrimidine. The p-type $C_{>3}N_4$ exhibited a remarkable photoactivity under visible light compared with pristine C_3N_4 , which is a stable n-type organic semiconductor deeply studied as heterogeneous photocatalyst for many environmental applications. The photoelectrochemical features of the synthesized p-type materials and pristine C_3N_4 were deeply investigated with chronopotentiometry and cyclic voltammetry, in the dark and under different illumination conditions, and then compared with the photocatalytic activity using 2-fluorophenol as substrate and different radiation sources. The p-doping with carbon of C_3N_4 reduces the band gap, slightly moves the potential of the valence band, and increases the conduction band to more positive potentials, thus precluding the application of these materials when large negative redox potentials are needed.

KEYWORDS. p-doped carbon nitride, visible light catalyst, p-type semiconductor, heterogeneous photocatalysis, water remediation.

1 INTRODUCTION

An attractive and challenging possibility to satisfy the increasing energy request of the world population and to develop technologies for the abatement of emerging pollutants is the exploitation of solar energy. Photochemical reactions that convert stable, low-energy chemical species into high-energy density species would produce fuels.[1] The most studied reactions are the H^+ reduction/ H_2O oxidation (water splitting reaction) [2] and the CO_2 fixation (artificial processes that mimic photosynthesis).[3] Many n-type semiconductors (SC) have been studied in detail, as photocatalysts or as support for co-catalysts for the oxidation side in the reactions described above. For example, the activation of carbon dioxide can be carried out electro- or photocatalytically, where the cathode of the electrochemical cell is modified by a molecular catalyst anchored on the cathode, typically metal-organic complexes covalently bound or adsorbed onto the SC surface.[4,5,6] The combination of n-type with p-type SCs is often needed.[7] However, most of the p-type SCs so far studied is inorganic.[8] The surface functionalization with metal-organic catalysts is easier on an organic SC. Organic p-type semiconducting polymers are reported in literature.[9] Unfortunately, they are affected by several drawbacks such as the low electronic conductivity, the low density of photogenerated charge carriers, the insufficiently negative redox potential of the conduction band, and the low chemical stability under photo-electrochemical conditions.[10]

The availability of organic p-type SCs, with a suitable conduction band potential for reduction, would allow an easy functionalization of their surface with many co-catalysts already developed.[11] Graphitic carbon nitride (“g-C₃N₄”) is a promising organic photocatalyst. g-C₃N₄ is a metal-free, medium-bandgap semiconductor ($E_g=2.7\text{eV}$), which partially absorbs into the visible region.[12,13] It exhibits many interesting properties, including production at low-cost and a unique thermal and chemical stability.[14] Its main drawbacks are the insufficient visible absorption (just in the violet-blue portion of solar spectrum),[15] and the low photocatalytic efficiency, due to the high recombination rate of the photogenerated electron-hole pairs. Graphitic carbon nitride is an n-type SC, although in literature it is sometimes used as a p-type SC.[16,17,18] The doping type of this material probably derives from structural and chemical modifications resulting from uncontrolled synthetic conditions. This work was focused on the optimization of the synthetic route [19] to produce carbon nitride with a stable p-type doping. The homogeneous substitution of carbon had been demonstrated to increase the visible light absorbance and electrical conductivity as well as surface area, thus enhancing both photooxidation and photoreduction activities. [20,21] The triaminopyrimidine precursor assures the direct incorporation of C in the structure. A deep photoelectrochemical investigation with chronopotentiometry and cyclic voltammetry, combined with photocatalytic degradation experiments, using different light source was carried out. This p-type SC can then be used directly as photocatalyst for abatement of pollutants and for possible assembly of hybrid catalysts (metal-organics functionalized, p-n heterojunctions).

2 EXPERIMENTAL

2.1 Chemicals and Materials

Triaminopyrimidine (T) (> 97%), melamine (M) (> 99%), tetraethylammonium chloride (TEACl) ($\geq 98\%$), tetrabutylammonium hexafluorophosphate (TBAPF₆) ($\geq 99.9\%$), 2-fluorophenol (2FP) (99%), and HNO₃ ($\geq 69\%$) were purchased from Sigma Aldrich. H₃PO₄ (85%) and DMSO (99.8%) were purchased from Carlo Erba, KNO₃ (for analysis, $\geq 99\%$) from Merck; acetonitrile and methanol (Chromasolv for HPLC, purity $\geq 99.9\%$) from Fisher/Honeywell. All chemicals were used without any further purification. Water was purified with a MilliQ plus apparatus (TOC = 2 ppb, conductivity 18.2 MΩ cm). During the synthesis and photo-electrochemical tests, N₂ or O₂ pure gases (> 99.9995%) were employed (Sapio, Turin).

2.2 Synthesis of n-type and p-type Carbon Nitride

All materials were synthesized through one-step thermal condensation, carried out in a horizontal modular tube furnace (LENTON, MOD. LHC 12/750/3216 TYPE 3216CC), under N₂ atmosphere, with temperature gradient of 5°C min⁻¹ until a plateau at 500°C, later maintained for 2 hours. Then a spontaneous cooling to room temperature followed under nitrogen purge. Before calcination, reagents were homogenized by grinding in an alumina crucible and then put in alumina boats (1 gram of precursor per boat, see Figure S1). Pristine n-type g-C₃N₄ was obtained from pure melamine. The C-doped carbon nitrides (C_{n>3}N₄) were obtained from calcination of grinded powders of melamine (M) and triaminopyrimidine (T) at different molar ratio. Precursors with an M:T molar ratio starting from 40:1 (2.5% T) up to 0:1 (100% T) were prepared. The synthesized material from a precursor with an x %mol fraction of T and (1-x)% mol fraction of M has been referred as “CNx”. For example CN75 indicates the material obtained from thermal condensation of 75% T and 25% M (or M:T = 1:3).

2.3 Exfoliation and fractioning

The raw powders obtained after the thermal treatment were suspended in pure DMSO (3 g L^{-1}) and treated for 2 hours in an ultrasound bath (Branson 2800) to exfoliate the grains of carbon nitride. Different size fractions were then obtained: a) allowing the exfoliated suspensions to settle naturally for different times: 0 min (no settling), 10 min (sufficient for sedimentation of the larger particulate), 1 day, 7 days; b) through centrifugation at $1800 \cdot g$ for 5 min, 10 min and 30 min (see Figure S2). The body of the supernatant was then separated from the settled particulate. The solvent was evaporated through a rotary vane pump. Then the powders obtained from the supernatant were washed five times with water to remove adsorbed DMSO and dried overnight at 60°C . The CN_x powders were named CN_x-zt, where -z suffix indicates the settling procedure and t the settling time. For natural sedimentation ($z=n$) and centrifugation ($z=c$), the time is reported in days and minutes, respectively, except when a different time unit is indicated in parentheses. For example "CN75-n1" indicates a powder from a CN75 raw material, exfoliated and then naturally settled for 1 day, "CN75-n10(min)" indicates a powder from a CN75 raw material, exfoliated and then naturally settled for 10 min, while "CN75-c5" is obtained after centrifugation for 5 minutes. The highly C-loaded samples (CN50, CN75 and CN100) were easily suspended even in pure water.

2.4 Electrode preparation

Transparent conductive supports (Corning® EXG alkaline earth boroaluminosilicate glass, $25 \times 25 \times 1.1 \text{ mm}$, Indium Tin Oxide (ITO) coated on one surface, $R_s = 9\text{-}15 \ \Omega$, Transmission $>80\%$) were purchased from Delta Technologies Ltd (USA). Glassy Carbon conducting supports (GCE) (SIGRADUR®G $25 \times 25 \times 3 \text{ mm}$, specific electrical resistance $45 \ \Omega \ \mu\text{m}$) were obtained from HTW (Germany). The electrodes were prepared following the doctor blade technique or by drop casting (see Figure S3). In the doctor blade procedure the ITO/GCE conductive support was coated by a layer of CN_x powder, suspended in few drops of N-methyl-2-pyrrolidone, and subsequently dried in oven at 80°C . In the drop casting procedure the ITO/GCE conductive support was covered by a layer of CN_x colloidal suspension, and then put in a temperature controlled self-built glass chamber. Under rotary vane pump suction, air continuously flowed into the chamber through a small hole on the top, accelerating the solvent evaporation. Both suspensions in H_2O and in high boiling DMSO ($T_{bp} = 190^\circ\text{C}$) were evaporated heating the chamber at 60°C , thus preserving the CN_x particles from degradation.

2.5 Materials characterization

The particle size and polydispersity were measured with an ALV-NIBS High Performance Particle Sizer (ALV GmbH) on diluted suspensions; the particle average hydrodynamic diameter was extrapolated at infinite dilution. The particle size was estimated at the infinite dilution limit to avoid errors caused by inter-particle attractive/repulsive interactions.[22] The autocorrelation functions were analyzed with the cumulants method, which is suited for particles with monomodal distribution.

The morphology of the raw and exfoliated powders was assessed through Scanning Electron Microscopy (SEM) by means of a Phenom-World Phenom Pro Desktop SEM, operating at 15kV. The raw powders were pressed onto a slice of carbon conducting tape. For exfoliated suspensions one drop was dried on a thin glass substrate, which was then fixed onto a slice of carbon conductive tape.

X-ray powder diffraction (XRD) patterns were recorded using a Philips PW 3830 diffractometer from PANalytical working in Bragg-Brentano configuration, equipped with a PW 3050 goniometer and a PW 3710 MPD control X-ray diffraction system. As X-ray source a high power ceramic tube PW3373/10 LFF

with a Cu anode (Cu- K_{α} radiation = 0.15418 nm) was used. The instrument was equipped with a Ni filter to attenuate K_{β} radiation. The radiation generator was operated at an accelerating voltage of 40 kV and at an applied current of 30 mA. The powder samples were hosted on a flat SiO₂ amorphous sample holder.

The diffuse reflectance spectra were recorded on homogenized powder layer with infinite optical length using a dual-beam Varian Cary 5000 UV-Vis-NIR Reflectance Spectrophotometer with an integrating sphere. The internal walls of the sphere were coated with polytetrafluoroethylene (PTFE) and BaSO₄ was used as reference material.

Different radiation sources were used (see the emission spectra in Figure S4). All radiation sources and optical interferential filters were purchased from Philips (Eindhoven, Nederland, see Figure S4). The Solarbox Sun simulator was purchased from CO.FO.ME.GRA., Milano. The lamps emission spectra and incident irradiance were recorded with a calibrated spectrum radiometer (Ocean Optics SD2000 CCD spectrophotometer, equipped with an optic fiber and a cosine corrector CC-3-UV-T). Different irradiation window spectra were used: 1) **UV** - narrow emission spectrum at 350-400 nm (Philips PL-S 9W/2P BLB fluorescent lamp, with an integrated irradiance on the entire emission spectrum of $11 \pm 1 \text{ W m}^{-2}$); 2) **UV-Vis** - range 340-800 nm (obtained through a Solarbox Sun simulator with a broad emission spectrum in the 340-800 nm range, without interposition of cut-off filters; integrated irradiance of $30 \pm 1 \text{ W m}^{-2}$ in the 340-400 nm range, integrated irradiance of $128 \pm 6 \text{ W m}^{-2}$ in the 400-520 nm range); 3) **Vis-wide** - range 400-800 nm (obtained through a Solarbox Sun simulator equipped with a 400 nm cut-off filter; integrated irradiance of $128 \pm 6 \text{ W m}^{-2}$ in the 400-520 nm range); 4) **Vis-Blue** - mid-wide emission spectrum between 400-550 nm, with an integrated irradiance of $30 \pm 1 \text{ W m}^{-2}$. A Phillips TLD 18W/18 BLB BLUE fluorescent lamp, $\lambda_{\text{MAX}} = 450 \text{ nm}$ with relevant narrow peaks at 406 nm and 438 nm and one small UV peak at 365 nm was used. A 400 nm cut-off filter interposed; 5) **Vis-Yellow** - mid-wide emission spectrum 520-650 nm. A Philips TL-D 18W/16 YELLOW fluorescent lamp with a $\lambda_{\text{MAX}} = 600 \text{ nm}$ and a relevant narrow peak at 550 nm was used.

The electrochemical experiments were carried out with a standard photo-electrochemical set-up, a computer-controlled potentiostat (PGSTAT12, Autolab), and a conventional three-electrode cell. The counter electrode (CE) was Pt sheet; the reference electrodes (RE) were Ag/AgCl/KCl (3 M) or Ag/AgCl/TEACl (0.1 M in CH₃CN); the electrolytic solution was aqueous 0.1 M KNO₃ or 0.1 M TBAPF₆ in CH₃CN, respectively, purged with N₂, or O₂ if needed. A 150 W Xe arc lamp was used as light source (LOT Oriel). Following collimation of the beam with lenses, the incident light intensity on the working electrode (WE), measured with a radiant power meter (Ocean Optics SD2000 CCD spectrophotometer), was $270 \text{ W m}^{-2}(\text{UV+Vis})$.

The photodegradation measurements were carried out using cylindrical Pyrex cells (4.0 cm diameter and 2.5 cm height, cut-off at 295 nm) on 5 mL of aqueous suspensions containing the photocatalyst powder (0.5 g dm^{-3}), $1 \times 10^{-4} \text{ M}$ 2FP and $1 \times 10^{-3} \text{ M}$ HNO₃. The suspensions were prepared by sonication for 1 minute and subsequently stirred in the dark for 2 hours to achieve the adsorption-desorption equilibrium between substrate and photocatalyst. Details on adsorption kinetics are reported in SI (see later). During irradiation the suspensions were magnetically stirred. After irradiation the suspensions were filtered through a 0.45 μm hydrophilic PTFE membrane (Millipore Millex-LCR) and analyzed by HPLC-UV (YL9300 HPLC System, Lichrospher R100 RP-18 5 μm column). The elution was carried out at 1 mL min^{-1} with 4.2 mM aqueous H₃PO₄:CH₃CN 65:35 in isocratic mode. The injection volume was 60 μL .

3 RESULTS AND DISCUSSION

3.1 Synthesis of p-type Carbon Nitride

The vast majority of the carbon nitrides is synthesized via a thermal treatment at 500–600°C through self-polycondensation of nitrogen-rich organic compounds, i.e. dicyandiamide, melamine, urea or cyanamide.[23,24] To induce the p-type doping, we increased the carbon content of the pristine C_3N_4 through calcination of grinded powders of melamine (M) and triaminopyrimidine (T) at different molar ratio. Then C-doped carbon nitrides ($C_{n>3}N_4$) were obtained. The synthesis is similar to that reported by Ho et. al., [19] who employed also triaminopyrimidine as co-precursor, because of its high structural similarity with melamine (M) (see Figure 1). They synthesized ($C_{n>3}N_4$) until a molar ratio T/M 1/9. The condensation of these two units should allow the insertion of carbon atoms directly into the molecular structure of the carbon nitride as postulated in Figure 1. In this work the molar ratio T/M has been extended until 100% T. Raw granular powders were obtained. As for C_3N_4 (and graphite), the stacking due to Van der Waals interactions between the single layers of carbon nitride makes it insoluble in most solvents.[25] The insolubility of carbon nitride is also due to its chemical inert character and to the absence of acid/basic groups in the conventional pH range (2-13). The carbon nitride grains were exfoliated in few hours with the concurrent use of ultrasonic irradiation and a proper solvent. Solvents like acetone, ether toluene, acetonitrile and THF were not effective in suspending the synthesized materials. The suspensions in protic solvents, like methanol, ethanol and water exhibited a more intense scattering, indicating that materials are largely suspended. Polar aprotic solvents with high dielectric constant, like DMSO, DMF, NMP (N-methylpyrrolidone), DMTU (dimethylthiourea) and HMPA (hexamethylphosphoramide) generated the best exfoliation results. DMSO appeared the best choice due to lower toxicity and cost. Anyway, the resultant suspension was quite heterogeneous. Then a gravity-induced separation was carried out, both with natural settling and centrifugation. The influence of the settling rate on different characteristics of the suspended fractions was then investigated.

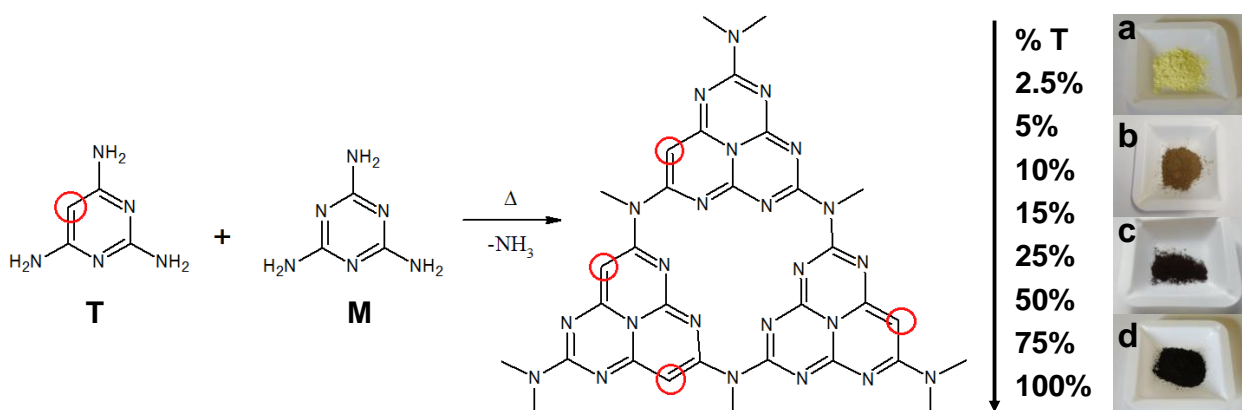


Figure 1. Postulated thermal condensation of melamine (M) and different %mol of triaminopyrimidine (T) to obtain C-doped carbon nitride. [19] On the right, pictures of some synthesized materials, grounded to powder (from top: pristine C_3N_4 , CN25, CN75 and CN100).

The exfoliation procedure produced smaller aggregates in the supernatant. Smaller aggregates are composed of sheets with much higher surface area and lower recombination of the photoproduced charge carriers as measured in photoelectrochemical experiments (see below). The photoelectrochemical features of the samples naturally settled for 1 week were close to those obtained after centrifugation (5 minutes at 1800·g). Thus here we report the properties of the 5 min-centrifuged

samples because their preparation procedure is considerably faster. The suspension of samples in water was more effective with larger C-loading (CN50, CN75, CN100) than for low C-doped materials or C_3N_4 .

3.2 Particles size and morphology

Dynamic Light Scattering (DLS) measurements were performed on the best material, CN75, after different settling times to estimate the size and polydispersity of the exfoliated particles. Each measurement was carried out on the supernatant diluted with pure DMSO, at different ratios (typically 1:5, 1:25 and 1:100). Suspensions naturally settled for less than one day showed large polydispersity, indicating a poor exfoliation and giving poorly informative results. Centrifuged or long-time settled fractions are characterized by particles with a monodispersed hydrodynamic diameter (see Table 1).

Table 1. Average hydrodynamic diameter measured for exfoliated particles of CN75 and CN100 suspended in DMSO.

SAMPLE	HYDRODYNAMIC DIAMETER
CN75-n1	155±5nm
CN75-c5	140±10nm
CN75-c10	115±10nm
CN75-c30	100±10nm
CN100-c5	155±5nm

The measured polydispersity indexes were $(PDI) \leq 0.1$. The results are also in close agreement with the CONTIN analysis (inverse Laplace transform analysis of the autocorrelation function, suited to analyze multimodal populations), confirming the high particle monodispersity. As expected, there was a regular trend between the decrement in particle size and the increment of centrifugation time. Surface topography obtained with AFM of ITO electrodes covered with a thin layer of CN75-c5 (electrodes used for the photoelectrochemical tests) revealed that particles size is approximately 400 nm (see Figure S5). Comparing this value with DLS results, an aggregation process occurs during solvent evaporation from the conductive support, and the particle size increases no more than 4 times.

Scanning electron microscopy (SEM) on the raw C_3N_4 and CN75 powders allowed comparing the size reduction of the particles and their change of morphology after exfoliation and fractioning. The particle diameter in the raw powders spanned from 3-5 μm to 50 μm (for C_3N_4) or 60 μm (for CN75), with an average size around 20 μm (Figure 2a, 2b, S6). The grains were porous (especially C_3N_4), suggesting that they are formed through aggregation of smaller particles. For both C_3N_4 -c5 and CN75-c5 samples (Figure 2c, 2d, S6), the exfoliation process dramatically reduced the particle average size to less than 1 μm , except for few residual bigger aggregates. The particle shape changed from big irregular clusters into thin and flat (almost transparent) sheets. As already mentioned, when the suspension containing these exfoliated sheets is drop casted for many cycles on the conducting support (ITO, GCE), the sheet aggregation occurs during the solvent evaporation.

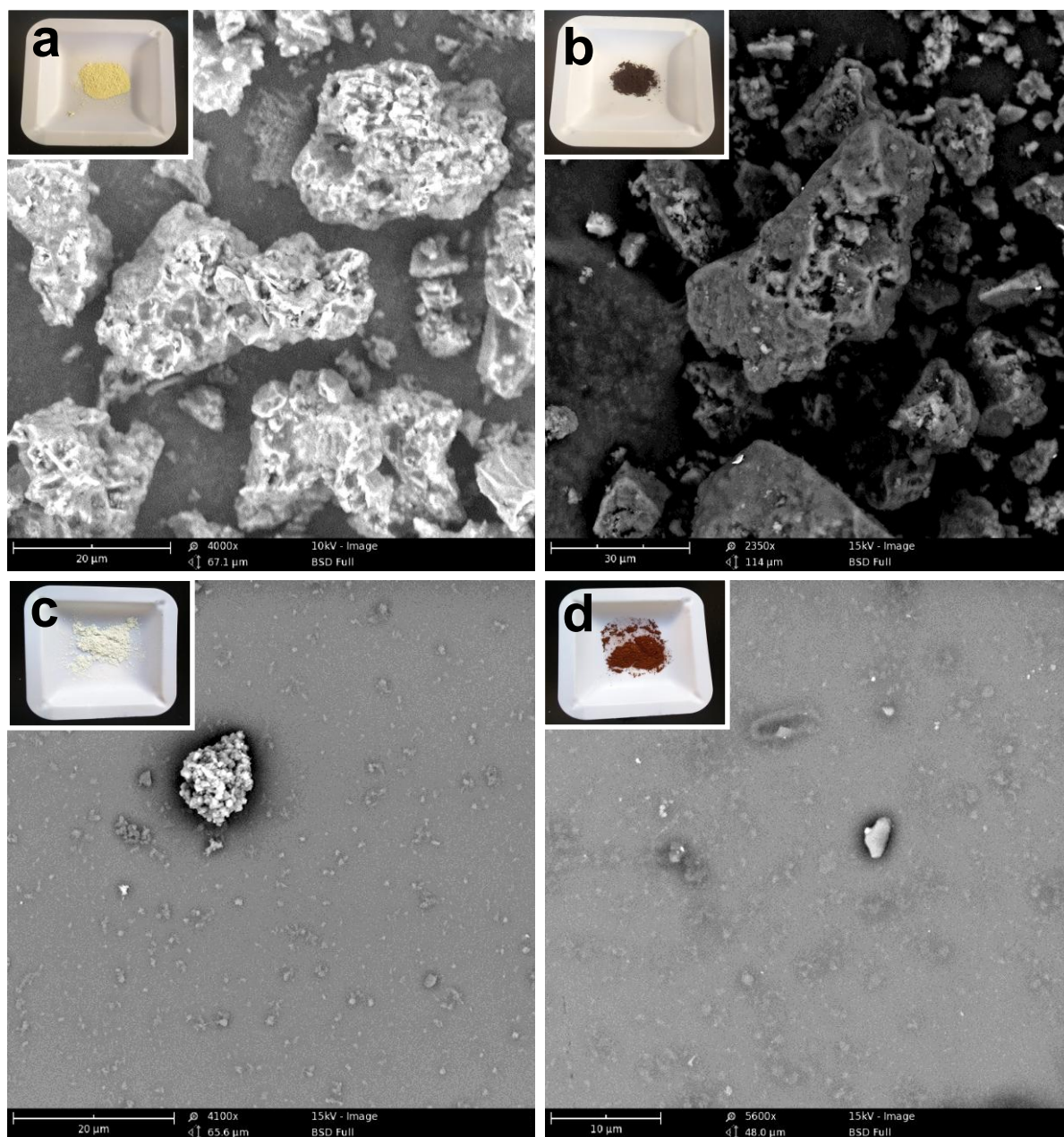


Figure 2. SEM pictures (a) raw C_3N_4 powder on carbon tape, (b) raw CN75 powder on carbon tape, (c) exfoliated C_3N_4 drop cast on glass, (d) exfoliated CN75 drop cast on glass. Insets: macroscopic appearance of the powder samples.

3.3 XRD characterization/X-Ray diffraction

The X-ray diffraction (XRD) patterns of the raw powders and exfoliated fractions obtained by solvent evaporation from the supernatant were recorded to clarify the structural evolution with the increase of C-loading and the progress of exfoliation. The interlayer distances (d_{hkl}) corresponding to the diffraction peaks were calculated from Bragg's law and were compared with data reported in literature. The intensity and position of the two diffraction peaks of the bulk C_3N_4 , synthesized from pure melamine, were in good agreement with those reported for pristine $g-C_3N_4$ (Figure 3a). The strongest diffraction peak at $2\theta = 27.07^\circ$ ($d_{hkl} = 0.328$ nm) well matched the literature values ($2\theta = 27.2-27.5^\circ$ or $d_{hkl} = 0.328-0.324$ nm), [24,26] and was assigned to the (002) plane diffraction corresponding to the characteristic interplanar stacking along the hexagonal c-axis of graphite-like materials. This stacking distance was slightly smaller than $d(002)$ values for exfoliated graphite (basal spacing 0.333 nm), natural flake

graphite (0.334 nm), highly ordered graphitic carbon or crystalline graphite (0.339 nm)[27] and it was significantly smaller than that of carbonaceous layered solids, like graphene (0.35 nm), randomly ordered (turbostratic) graphite (0.36-0.38 nm) and graphene oxide (0.678 nm)[28]. The higher packing density observed with C_3N_4 is due to the localization of the electrons, caused by substitution of carbon with nitrogen atoms in the aromatic structure, and the consequent stronger inter-layer interaction. A second less intense peak was located at $2\theta = 13.06^\circ$ ($d_{hkl} = 0.677$ nm). Similar values were reported in literature ($2\theta = 13.0-13.3^\circ$ or $d_{hkl} = 0.681-0.665$ nm), which were differently explained by various authors.[24,29] The peak can probably be ascribed to the (100) diffraction planes, corresponding to an in-plane periodicity, i.e. to the hole-to-hole distance in the sheets of nitride pores (tri-s-triazine units). The absence of sharp peaks in the XRD pattern indicated a low regularity in the stacking of the tri-s-triazine units in the domains.

The 2θ position of the XRD peaks remained unaffected for samples with low C-loading ($\leq 10\%$, CN10, see Figure 3a), indicating that the incorporation of carbon did not damage or greatly modify the host structure of g- C_3N_4 . The peak at $2\theta = 13.2^\circ$ gradually decreased with the carbon loading, suggesting that the in-plane periodicity is progressively lost. The intensity of the peak at 27.2° also markedly decreased, broadened and shifted with the increase of the carbon content, indicating a lower regularity of the inter-planar stacking along the hexagonal c-axis. The CN50, CN75 and CN100 samples showed only one distinct broad peak, whose maximum slightly shifted to lower values ($2\theta = 26.78^\circ$, 26.65° and 26.50° , corresponding to $d_{hkl} = 0.333$ nm, $0.334-5$ nm and 0.336 nm, for CN50, CN75, and CN100, respectively). According to the average inter-planar distances obtained and literature values cited above, the heavy C-loading progressively induced a transition from C_3N_4 domains to graphitic domains. Figure 3b reports the XRD patterns recorded for the CN75 powder after exfoliation and fractioning. Small differences appeared between CN75-n10(min) and raw CN75 powders. On the contrary, the CN75-c5 sample exhibited a significant decrement of the interlayer stacking peak, demonstrating that the bulk layered material was successfully exfoliated into smaller particles and 2D nanosheets, as also confirmed by SEM investigation.

3.4 Diffuse Reflectance (DR)

The UV-Vis-NIR absorption spectra of the C_3N_4 and CNx raw powders are reported in Figure 3c. At any λ there was a reflectance decrement (increment of absorption) with the increase of the C-content. This behavior can be explained both in terms of the gradual narrowing of the energy band gap and the increasing density of intra-gap trap states.

A set of measurements was performed on the CN50, CN75 and CN100 samples after exfoliation and fractioning. In Figure 3d, the comparison between the spectra of raw CN75 and CN75-n10(min) reveals almost the same features previously confirmed by XRD. The less exfoliated samples showed a lower absorption in the whole spectrum up to 600 nm. On the other hand, the spectra of the smallest particles (CN75-n1 and CN75-c5) were remarkably different compared with the previous ones. The absorption plateau (near 500 nm) blue-shifted of about 100 nm. As for larger particles the extinction can be assigned to the reduced scattering, for the smaller particles the observed extinction cannot be explained just in terms of different particles size, but reflects also different electronic properties.

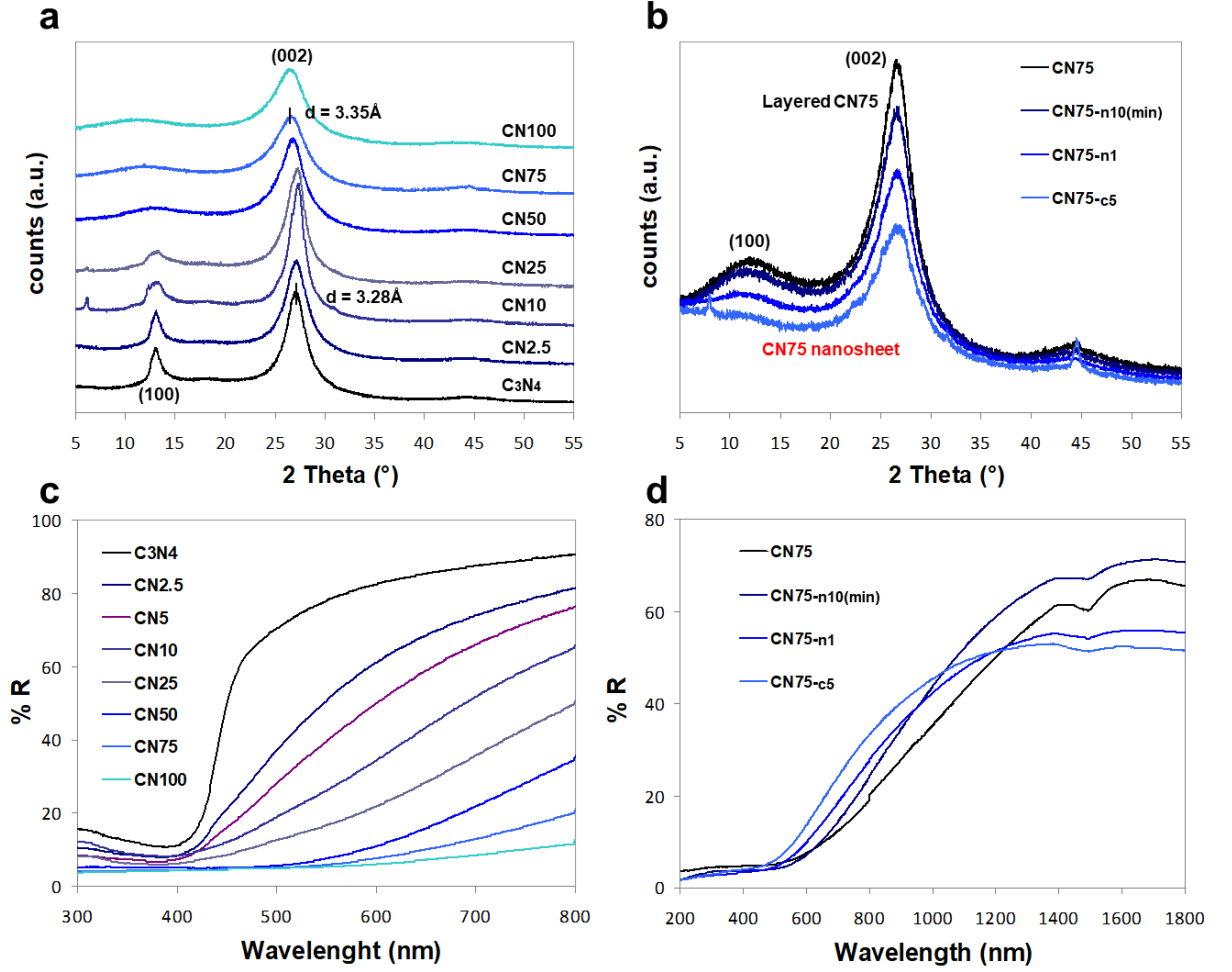


Figure 3. X-Ray diffraction patterns and Diffuse Reflectance (DR) spectra of the synthesized materials. a) XRD of raw C_3N_4 and CN_x powders, with x from 2.5 to 100; b) XRD of CN75 samples after exfoliation and different settling times: 0 min (raw powder), 10 min (CN75-n10(min)) and centrifugation (CN75-c5 at 1800·g); c) DR spectra of raw C_3N_4 and raw CN_x powders, with x from 2.5 to 100; d) DR spectra of CN75 samples after exfoliation and fractionation for different times, i.e. samples CN75, CN75-n10(min), CN75-n1, and CN75-c5.

The energy band gap E_g of the synthesized materials was evaluated by means of Eq.1 that relates the optical absorption coefficient α and the photon energy $h\nu$ for semiconductors: [30]

$$\alpha h\nu = A (h\nu - E_g)^n \quad (\text{Eq.1})$$

where A is a proportionality constant and $n = 1/2$ for a direct allowed transition, $n = 3/2$ for direct forbidden transition, $n = 2$ for allowed indirect transition, $n = 3$ for forbidden indirect transition.[31] Eq. 1 was used in a Tauc plot,[30] where $(\alpha h\nu)^{1/n}$ is plotted against the photon energy $h\nu$. The attenuation constant in transmission α for powders is calculated from the reflectance spectrum. Both the Kubelka-Munk (K-M) function $F(R_\infty)$ or the apparent absorbance $[\log(1/R_\infty)]$ are proxies for the actual absorption spectrum.[32] The absorption curve drawn from reflectance data reflects the real spectrum only if the scattering coefficient is independent on the wavelength, i.e. when the average grain size is large compared with the incoming wavelength. Since the exfoliated sheets are smaller or comparable with the incoming λ , the best way to estimate α is through the following equation:[33]

$$\alpha_\nu = \frac{1}{2} d \ln[(R_{MAX} - R_{min})/(R_\nu - R_{min})] \quad (\text{Eq. 2})$$

where d is the sample thickness, R_{max} and R_{min} are the maximum and minimum values of DR, respectively, in the recorded spectrum and R_v is the DR value for any intermediate energy photons. According to Eq. 1, in a Tauc plot the linear extrapolation to $(\alpha hv)^{1/n} = 0$ of the exponentially raising part of the curve gives the optical energy gap of the material. Similarly, in our case $\ln[(R_{MAX} - R_{min}) / (R_v - R_{min})]^{1/n}$ was plotted against hv to calculate the semiconductor E_g (see Figure S8, S9).

However, for an unknown material the type of transition cannot be assumed *a priori*. Then a wrong choice of the n value can affect the calculated E_g , as it depends on the chosen n (see Table 2). On the one hand, the cyclic voltammetry (CV) can provide an estimation of the optical band gap (as the difference between the valence band and conduction band potentials, see below), by which according to Eq.1 the actual optically induced transition mechanism (value of n) could be selected. On the other hand, the fluorescence emission intensity of the materials, which can be observed under a 365 nm UV lamp, can facilitate the choice of n , because a strong emission is generally related to a direct allowed transition ($n = 1/2$), and the absence of fluorescence to indirect transitions ($n = 2$ or 3).

Table 2. Optical Band Gap (E_g in eV) estimated from interpolation of the DR spectra of the synthesized powders, calculated for different possible optical transitions (different exponent n in the Tauc equation). The qualitative fluorescence emission intensity and the estimation of E_g from cyclic voltammetry helped the choice of the correct n value for each material. The values of E_g calculated from Tauc plots that are consistent with E_g evaluated from CV and fluorescence emission are outlined with the cyan background. Then not only E_g but also the optical transition mechanism changed with the carbon content.

Sample	E_g (n=1/2)	E_g (n=3/2)	E_g (n=2)	E_g (n=3)	E_g from Cyclic Voltammetry	Fluorescence emission
C ₃ N ₄	2.78	2.65	2.59	2.46	2.8	Yes, strong
CN2.5	2.78-2.94	2.62	2.47	2.14	/	Yes, strong
CN5	2.74-2.92	2.65	2.43	2.10	/	Yes, ~ strong
CN10	2.71-2.94	1.37 / 2.72	1.15 / 2.38	0.75 / 2.42	/	Yes
CN25	2.63-2.90	1.23 / 2.60	0.98 / 2.16	0.72 / 2.26	~ 1.7	Yes, weak
CN50	2.39	0.93 / 1.72	0.85 / 1.14	0.62	> 1.1	No
CN75	1.81-1.92	0.81 / 1.05	0.72	0.34	> 0.7	No
CN75-n10(min)	2.11-2.20	0.94 / 1.36	0.80 / 1.09	0.54	~ 0.8	No
CN75-n1	2.17-2.61	0.98 / 1.48	0.87 / 1.18	0.65	1.0-1.3	No
CN75-c5	2.24-2.75	1.00 / 1.54	0.91 / 1.22	0.71	1.2-1.3	No
CN100	1.73-1.97	0.62 / 0.89	0.50	0.06	~ 0.6	No

Accordingly, Table 2 reports the E_g range evaluated under possible types of transition (different n), the estimation of E_g from cyclic voltammetry and the qualitative evaluation of fluorescence emission. When different interpolations on the DR spectra led to similar values, a range is reported, otherwise two distinct E_g values are presented separated with a slash. Moreover, CVs carried on mid-highly C-rich samples led sometimes to different E_g values (reported in Table 2 as E_g ranges). This data dispersion is

due to the synthetic procedure that cannot be finely controlled, producing materials with slightly different structure and energy states in different batches.

The energy gap of pristine $g\text{-C}_3\text{N}_4$ ($E_g = 2.78$ eV), obtained from the Tauc plot with $n=1/2$, is in close agreement with the CV measurements and the strong fluorescence emission observed. Accordingly, the transition mechanism is direct allowed ($n = 1/2$). In the case of the CN2.5 and CN5 samples (low C-loading), the E_g value from CV cannot help to distinguish uniquely the transition mechanism, because CV is also sensitive to the trap states. The strong fluorescence emission suggests that $n=1/2$ is still the correct choice. The resulting E_g value is almost unchanged compared with $g\text{-C}_3\text{N}_4$, suggesting that the formation of many trap states observed in DR does not affect the VB and CB position. In the case of CN10 and CN25 (mid C-loading), the high density of trap states formed in the band-gap makes difficult to distinguish them from the band edges (see Figure S9). The E_g value measured from CV together with the (weaker) fluorescence emission observed suggests either a direct forbidden mechanism ($n = 3/2$) or a direct allowed transition, with subsequent non radiative recombination through trap states. The high C-loading samples, CN50 to CN100, are characterized by the absence of fluorescence emission, which suggests an indirect transition. The comparison with the CV data indicates that an allowed mechanism ($n = 2$) is consistent for all the materials. In these cases there is a high density of trap states in the band-gap. In addition, E_g values vary from about 0.7 eV to more than 1 eV (assuming $n=2$), for raw CN75 and exfoliated CN75-c5, respectively. Then the E_g values progressively increased with the increase of settling time. Eventually, a regular trend between the increment of C-loading and the decrement of E_g (both calculated from DR data and measured with CV) was observed, with the concurrent change of the optical transition induced by the increase of the density of intra band gap trap states.

3.5 Photo-electrochemical measurements

The most relevant photoelectrochemical features of the material synthesized were investigated through Cyclic Voltammetry (CV) and Chronopotentiometric (CP) measurements, in the dark and under illumination under **UV-Vis** (see Experimental section, unless differently stated), carried out on ITO electrodes coated with the drop casting method with suspensions of pristine C_3N_4 or CN x in DMSO. The CPs were carried out in aqueous solution to determine the valence and conduction band potentials of the materials (conditions in Figure 4 caption). CVs were carried out on glassy carbon electrodes (GCE) (conditions in Figure 4 caption). GCE was preferred because of its higher affinity with CN x samples and its stability at negative potentials (up to -2 V vs NHE), where ITO cannot work because it suffers decomposition (reduction of Sn^{4+} at -1V vs NHE).

The open circuit potential (OCP) recorded in a CP corresponds to the Fermi potential of the cell. The photopotential is the ΔV recorded in dark conditions against irradiation. Under illumination, the Fermi potential of C_3N_4 moved to more cathodic values (Figure S10) due to the photo-induced electron accumulation on its CB, indicating a n-type behavior. On the contrary, a p-type behavior corresponds to a photo-induced accumulation of holes in the SC valence band (VB), with the consequent development of a more anodic potential under illumination. The CP measurements on samples with low C-loading (CN2.5, CN5, CN10, CN25) did not exhibit any stable p-type doping, as low and unstable photopotential values < 50-70 mV were measured and a rapid photo-induced deactivation was observed.

The samples with larger C-loading (CN50, CN75, CN100) and different exfoliated fractions showed more interesting electrochemical properties. The CN50 sample exhibited a stable p-type doping, with photopotential near 150 mV (see Figure S10), reproducible for an extended time under irradiation before deactivation. Moreover, the potential increase under irradiation was fast as well as the drop in

the dark, indicating a fast generation of e^-h^+ pairs together with a fast undesired recombination of the photoproduced charge carriers. On the contrary, within the CNx series the CN75 sample exhibited the most intense p-type behavior, reproducible and quite stable over the time. The comparison between the CPs in Figure 4a underlines the key role of the settling time on the photo-electrochemical behavior of the materials studied. The powder obtained from a suspension of exfoliated CN75, settled for 10 minutes, exhibited a poor p-type behavior. From the same CN75-n1 batch, the powder obtained from the supernatant showed a strong p-type behavior, with a photopotential > 300 mV. The optimal centrifugation time needed to obtain the best photoresponse was 5 minutes at 1800·g. The powder recovered from the supernatant showed a 600 mV photopotential, with a dramatically reduced photogenerated charge carrier recombination rate. An exfoliated suspension settled naturally for 5-7 days displayed similar features. In Figure 4a the photoresponse increased and the recombination rate of the photogenerated charge carriers decreased with the increase of the sedimentation time, while the p-type doping was preserved. At longer centrifugation time, the results were similar, but the recovered amount of the sample was truly low. Also the CN100 sample showed a reproducible p-type behavior, quite stable over the time, as well as the already observed dependence of the photo-electrochemical activity on the sedimentation time. CN100 and CN100-c5 showed photopotentials around 10-30 mV and 350 mV, respectively (see Figure S10 c,d), lower than CN75.

Figure 4b reports the comparison between the CVs carried out on exfoliated CN75 in two different conditions. In the first case, GCE/CN75-n1 was used as working electrode and different peaks emerged both in reduction and in oxidation, corresponding to the potential of the conduction band (CB -0.5 V) and the valence band (VB +0.8 V), respectively. In the second case, a slurry of CN75-n1 in DMSO (0.1 mg mL⁻¹, with addition of 0.1 M TBAPF₆ as supporting electrolyte) was studied using a GCE plate as working electrode. Even in this case, the reduction and oxidation peaks were detected. Their potential was in agreement with the first measurement because for CB and VB they were -0.6 V and +0.4 V, respectively. The discrepancy observed between the two measurements depended on the intrinsic different experimental conditions. In the first case the material was in direct contact with the conducting support and the electron transfer from the photoexcited CN75 layer was somehow easier compared with the GCE plate immersed in the CN75 slurry. The contribution of the GCE plate and the solution (0.1 M TBAPF₆ in CH₃CN or DMSO) to the overall signal has been subtracted (see Figure S11) so that just the current coming from the CN75 layer is here reported in both cases.

As the fractionation discriminated the particles by size, and the XRD and DR spectra together with CV and CP measurements showed that the physical-chemical properties are closely related to the size, the strongest photopotential and p-type behavior was exhibited by well exfoliated sheets of CN75.

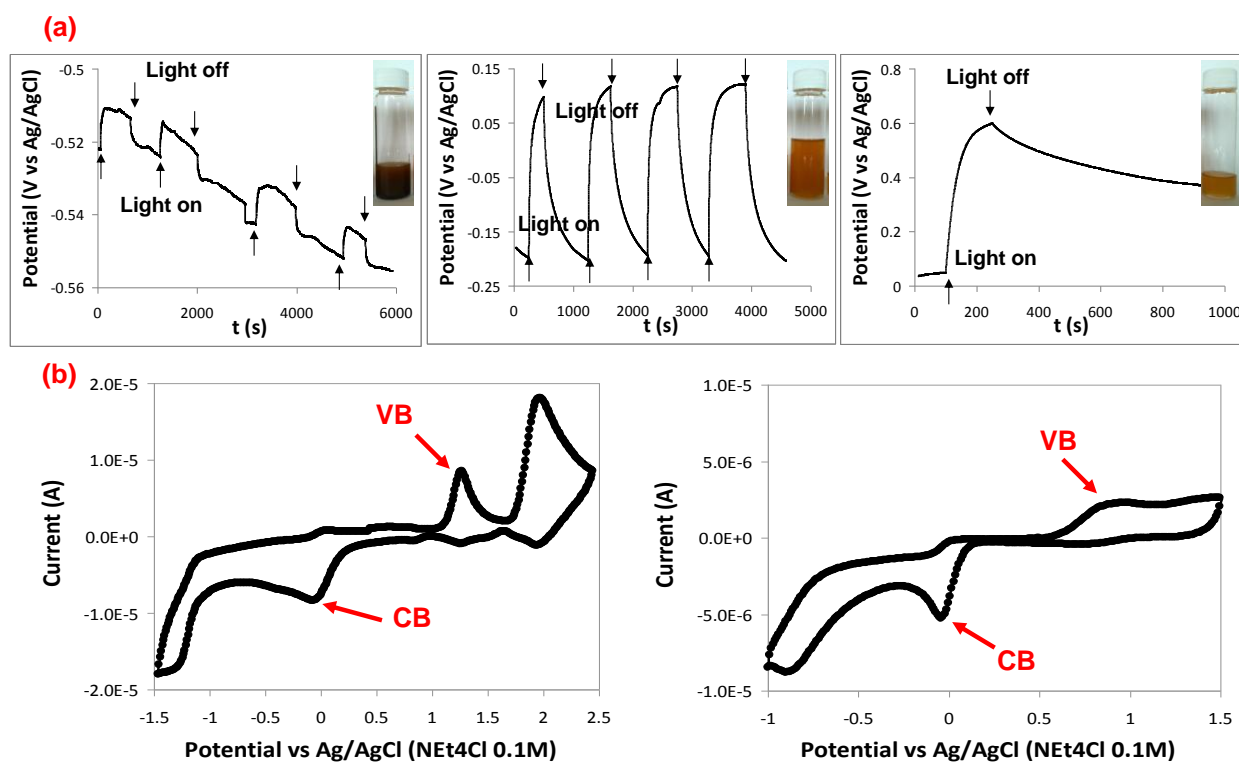


Figure 4. a) Chronopotentiometry under dark/*UV-Vis* blight cycles in 0.1 M KNO₃, under N₂ atmosphere, pH=7, using Ag/AgCl (in 3 M KCl) as RE and Pt as CE, WE: ITO/CN75, *UV-Vis* conditions. Left: CN75-n10(min), photopotential (OCP) 10 mV; Center: CN75-n1, OCP >300 mV; Right: CN75-c5, OCP 600 mV. Inset: exfoliated CN75 suspensions used to fabricate the electrodes. b) Cyclic Voltammetry with 0.1 M TBAPF₆ in anhydrous CH₃CN, under N₂ atmosphere in the dark. Other conditions were: Ag/AgCl /NEt₄Cl 0.1M in CH₃CN (-0.86V vs Fc/Fc⁺, S9f) for RE, and Pt plate for CE, scan rate 0.2 V s⁻¹. Right, WE: GCE plate, measurement in a slurry of CN75-n1 in DMSO (0.1 mg mL⁻¹) with 0.1 M TBAPF₆. Band gap > 0.9 eV, CB: ≈ -0.05 V, VB: ≈ +1.2 V.

Table 3. Summary of the most important photoelectrochemical properties of the most relevant CN_x-zt materials under *UV-Vis* irradiation. The potential values are referred to Ag/AgCl (3 M KCl), and those with (*) to Ag/AgCl/NEt₄Cl 0.1M in CH₃CN (-0.86V vs Fc/Fc⁺).

Sample	Photo-photopotential (mV)	Fermi pot (V)	VB pot* (V)	CB pot* (V)	Flat band potential (V)	Charge carriers density (cm ⁻³)	Majority carrier halftime (s) under N ₂	Majority carrier halftime (s) with O ₂
C ₃ N ₄	300	+0.1	+1.6	-1.2	-0.42	1.0 10 ¹⁶	170-830	120-370
C ₃ N ₄ -c5	350 - 450	+0.1	+1.6	-1.2	-0.58	1.6 10 ¹⁶	830-5000	280-560
CN75-n1	300 - 350	-0.25 / -0.2	+1.1±0.2	-0.1±0.05	+0.46	1.2 10 ¹⁶	100-560	140-770
CN75-c5	550 - 600	+0.0 / +0.1	+1.2 ±0.1	-0.0±0.05	+0.74	2.7 10 ¹⁶	430-1400	560-2500
CN100-c5	350	+0.2	+1.1	+0.1	+0.63	1.6 10 ¹⁶	620-5000	830-9800

Table 3 reports a summary of the most important features of the most relevant materials synthesized, derived from the photo-electrochemical measurements described above. The details of the experimental procedure are outlined in Figure S12. The Fermi potential (OCP) was obtained from the flat

part of the CP in the dark. The photopotential was calculated subtracting the potential values of the two flat parts of the CP, under illumination and in the dark, respectively. The CB and VB potentials were obtained from the CV measurement, as already described. The flat band potential was estimated through a CP in the conditions described above, with sequential additions of a secondary carrier scavenger in the solution (O_2 in the case of p-type CN75 and CN100, methanol in the case of n-type C_3N_4) and increasing the incident light irradiance (see Figure S12 d). The photogenerated charge carrier density in the materials was calculated integrating the current values of the CV in the potential range delimited by the OCP values obtained from a CP, in the dark and under irradiation, respectively, [34] under the same conditions described for the CV (Figure S12c). Finally, the charge carriers half time was calculated from the CP in N_2 , during the dark half-cycle after illumination, through the fit of the logarithm of the exponential decay of the OCP value (Figure S12 b). Both the inverse of maximum (initial) and minimum (final) slope values of the curves are reported in Table 3, column 8. The same calculation was then repeated with a CP on the same material under bubbling of O_2 as an electron scavenger (Table 3, column 9). The molecular oxygen reacted with the photogenerated secondary charge carriers in p-type SCs like CN75, increasing the lifetime of the h^+ in the VB (resulting in a slower recombination rate under O_2 , see Figure S12 b). Conversely, for n-type C_3N_4 the photogenerated primary carriers are electrons, and their lifetime in the CB was reduced because of the reaction with O_2 .

In conclusion, we observed that the exfoliation does not affect the bands position, whilst it increases the photopotential, the charge carrier density and the majority carrier lifetime. In addition, as expected, the flat band potential for the n-type C_3N_4 is more negative compared with p-type CN75. The relevant features of the new materials are schematized in Figure 5. The p-doping of C_3N_4 with carbon reduces the band gap, it slightly moves the potential of the valence band, and shifts the conduction band to more positive potentials. The doping with an uncontrolled (small) amount of C produced similar effects.[35]

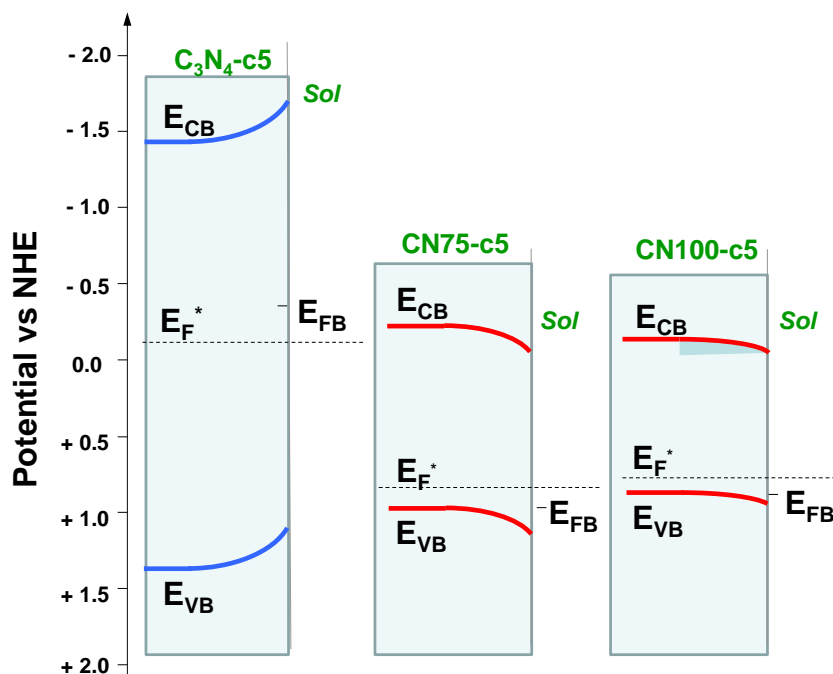


Figure 5. Band energy position of C_3N_4 , CN75 and CN100. Data of Table 3, column 4,5 for CB and VB are referred to NHE. The data obtained in 0.1M TBAPF₆ in CH₃CN are shifted by -0.23 V, and those obtained in 0.1 M KNO₃ are shifted by 0.208 V.

The CP response of CN75-c5 under different light sources is reported in Figure 6. Photons with $\lambda > 520\text{nm}$ (**Vis-Yellow**) do not induce any significant photopotential in the material (less than 50 mV). This light source is then expected to scarcely induce any photocatalytic activity. The **UV-Vis** and **Vis-Blue** lamps (curves 1 and 2, respectively) are able to induce almost the same absolute photopotential but, in the latter case, the potential rise is remarkably slower. The same photopotential indicates that both the irradiation conditions are able to carry out the same electrochemical reactions. The lower potential rise recorded under blue light implies a less efficient separation of charge carriers, leading to a slower reaction rate.

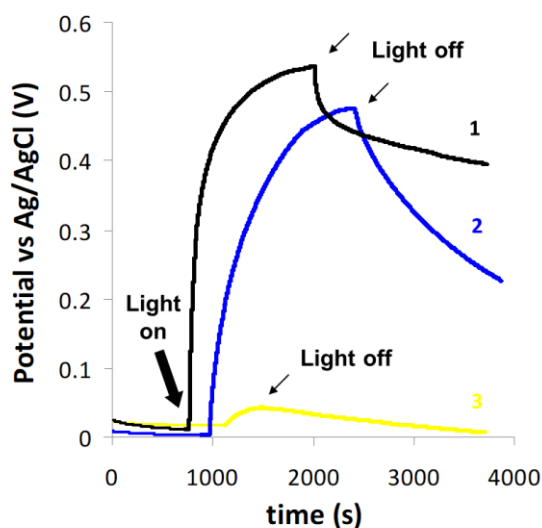


Figure 6. a) Chronopotentiometry under a dark/light cycle for CN75-c5 with different light sources: 1) UV-Vis (see text), 2) Vis-Blue, 3) Vis-Yellow. Conditions: 0.1 M KNO_3 , N_2 atmosphere, $\text{pH}=7$, RE: Ag/AgCl (in 3 M KCl), CE: Pt, WE: ITO/CN75-c5.

3.6 Photocatalytic activity

The photocatalytic activity of pristine C_3N_4 and CN75, exfoliated and after different settling times, was evaluated through the degradation under irradiation of a model substrate. We chose 2FP because it does not absorb at $\lambda > 300\text{ nm}$ (Figure S13 a), where all the used radiation sources are emitting. In addition, it can undergo both oxidation (+1.1 V vs Ag/AgCl) and reduction (-0.1 V vs Ag/AgCl, Figure S13 b). Considering the good matching of these potentials with the VB and CB of both C_3N_4 and CN75, 2FP could act both as electron and hole scavenger during the photodegradation. As the extinction spectra of the synthesized materials are quite different (Figure 3c), we investigated the excitation of these specimens under visible light and, in particular, the range of wavelengths where they were more photoactive. Therefore we needed to employ different radiation sources, as described in the Experimental section.

A preliminary test was carried out in air under the **Vis-Yellow** source, where C_3N_4 does not absorb and no photoactivity is expected. Conversely, CN75 strongly absorbs at these wavelengths. However, we just observed negligible degradation of the substrate with CN75 (<10% at 20 h, see Figure S14 c), according to the scarce photopotential measured before (Figure 6). The absorption of CN75 in the 520-650 nm range is probably due to localized trap states, not able to form long-living charge carriers. The light absorption at a given λ is a necessary condition for a material to be photoactive, but the photogenerated charge carriers must have a lifetime sufficient for their migration and reaction at the

surface. The absorption due to the localized trap states does not increase the photoactivity because of the fast recombination. Given that the photocatalytic activity is negligible, the irradiance of the various light sources at $\lambda > 520$ nm was not considered. The photoactive range for CN75 must then be localized at $\lambda < 520$ nm despite its strong absorption until the NIR spectrum.

The same photodegradation tests were carried out also in air under **UV-Vis** conditions, as already done during photoelectrochemical investigation. These experiments were carried out mainly to compare the activity in the presence/absence of oxygen. The pristine C_3N_4 (n-type) exhibited a good photoactivity, with a higher degradation rate compared with CN75 (p-type). The photoactivity was also measured under N_2 atmosphere. (see Figure S14 d), where the degradation rate was lower than in air, but, this time, larger for CN75 compared with C_3N_4 . Since a much faster degradation of the substrate occurred when oxygen was present, with both C_3N_4 and CN75, O_2 operates in both cases as a good electron scavenger, and 2FP is degraded mainly directly or indirectly via oxidation through species related to VB charge carrier. The actual degradation pathways were not studied in detail here, because old literature is present on the subject.[36] When oxygen was not present, the reductive path of the 2FP degradation was possible. n-Type C_3N_4 suffered more the charge carrier recombination, due to accumulation of primary carrier (electrons) in the CB. In a p-type C_3N_4 , holes are the majority carriers, whose accumulation was reduced by their reaction with the organic substrate, according to the conclusions reached above on the lifetime of majority carriers in the absence of an organic scavenger. However, the different absorption of C_3N_4 and CN75 could also affect the observed photoactivity, because C_3N_4 absorbs at $\lambda < 450$, whilst CN75 over the entire **UV-Vis** spectral window (see Figure 3 c and Figure S4).

Then, the photocatalytic degradation tests of 2FP were carried out using 3 different ranges of illumination, namely **UV**, **Vis-Blue** and **Vis-wide**, to assess the possible visible activity of the synthesized carbon doped C_3N_4 (Figure 7). The initial degradation rate (obtained as $\text{rate} = k_{\text{kin}} C_o$, where k_{kin} was obtained from the decay of the initial concentration C_o) is reported in Table 4 together with the irradiance, both in $W m^{-2}$ and moles of photons s^{-1} , in the active range. The active range was defined as the actual range in which the specific catalyst absorbs and shows a non-negligible photoactivity.

The photodegradation tests in air under **UV** irradiation with C_3N_4 -c5 and CN75-c5 (see Table 4 and also Figure S15) suggested that the most photoactive material is C_3N_4 while CN75 is remarkably less active. The rate using P25 for several monofluorophenols, including 2-FP was reported.[36] Although the conditions are different, and in particular the light intensity is 60 times larger for P25 and its concentration is 5 times lower, the rate with P25 is only 5 times larger than that of C_3N_4 under UV, suggesting that the synthesized C_3N_4 is a good photocatalyst. The photon efficiency, calculated from the ratio between the rate and the photon flux in the cell was remarkably high for C_3N_4 (40%), and decreased to 5.8% in the presence of CN75. The rate for CN75 was almost 1/7 of that of C_3N_4 (Figure 7 a). Since the absorption of the two materials in the **UV** range is almost the same (see DR spectra), the lower CN75 photoactivity is probably due to a higher recombination rate. The photoactivity of C_3N_4 and CN75, settled for different times (1 day against 5 min centrifugation), was also compared (Figure S15). Coherently with electrochemical evidences, the degradation rate increased with longer settling time, and the most exfoliated sheets exhibited better photoactivity.

Table 4. Irradiance of the radiation sources employed (W m^{-2}) and their corresponding values in mol photon s^{-1} in the cell and in different spectral windows. The column “Rate” reports the initial rate for the photodegradation of 1×10^{-4} M 2FP in the presence of C_3N_4 -c5 and CN75-5c; in the last column the normalized rates (rate/I_0) are reported.

^(a) “Active range” is the actual irradiation window where the catalyst considered absorbs.

	Radiation source	Active range (nm) ^(a)	Irradiance (W m^{-2})	Photon flux I_0 ($\text{mol photons s}^{-1}$)	Rate (mol s^{-1})	rate/I_0
n-type	UV	340-400	11.0	4.32E-08	1.74E-08	8.37E-05
	Vis-Blue	400-450	16.4	7.49E-08	6.30E-10	2.30E-06
	Vis-wide	400-450	20.6	9.52E-08	6.95E-10	2.25E-06
p-type	UV	340-400	11.0	4.32E-08	2.51E-09	1.21E-05
	Vis-Blue	400-520	36.3	1.73E-07	1.45E-09	3.48E-06
	Vis-wide	400-520	128	6.33E-07	2.22E-09	2.78E-06

Photodegradations under **Vis-wide** irradiation in air with C_3N_4 -c5 and CN75-c5 (Figure 7 c) showed a photon efficiency remarkably lower than under UV, namely 0.7% and 0.35% for C_3N_4 and CN75, respectively. However, considering the degradation rates, CN75 was more photoactive compared with C_3N_4 (ratio of rates is 3.2). The absorption in the Vis range is central for CN75. The test performed under **Vis-Blue** irradiation (Figure 7 b), where both the materials absorb, showed that the photon efficiency is almost the same (0.8%), but CN75 resulted the most photoactive material, with a rate ratio of 2.3 compared with C_3N_4 . Given the emission spectrum of the lamp, centered at 450 nm (see Figure S4), the C_3N_4 absorbs only half of the lamp spectrum (onset of absorption approximately 450 nm), whilst CN75 absorbs at all the wavelengths of irradiation, explaining the higher rate observed. In all the tests the centrifuged materials resulted more photoactive compared with the settled ones, i.e. C_3N_4 -n1 and CN75-n1 (Figure S15).

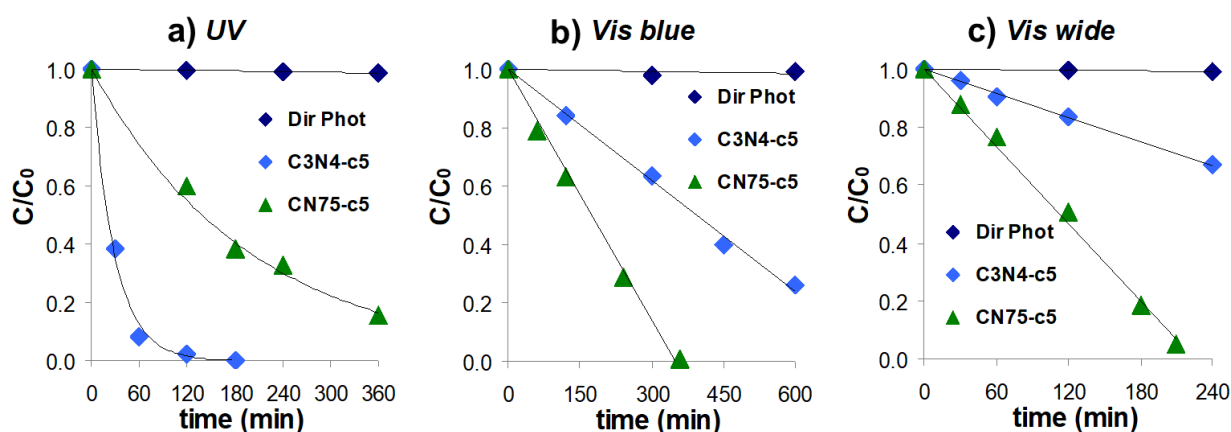


Figure 7. Photodegradation of 2PF in the presence of C_3N_4 -c5 or CN75-c5, under (a) **UV**; (b) **Vis-Blue** and (c) **Vis-wide** conditions. Direct photolysis is indicated as Dir Phot. Conditions are reported in the text.

Normalization between the rate and the irradiance, whose value is quite different for the various radiation sources, was then performed. This allowed comparing the degradation rates independently on the irradiation intensity and then to estimate the different photoactivity of the materials under UV and visible spectral ranges. We employed the standard kinetic model proposed by Minero *et al.*, because it was validated under several experimental conditions.[37,38] Following this kinetic model, the rate depends on the square root of light irradiance. The irradiance values were calculated, as required, in mol of photons s^{-1} for different active ranges of wavelength and the rates were normalized accordingly. Concerning C_3N_4 , the visible portion considered active was restricted at $\lambda < 450$ nm, the onset of absorption. In the case of CN75, the active range was extended until $\lambda = 520$ nm, considering the negligible photoactivity emerged from the preliminary test and CP under the Vis-Yellow source. All the normalized data for C_3N_4 -c5 and CN75-5c are reported in the last column of Table 4.

C_3N_4 exhibited a normalized photocatalytic activity under **UV** nearly 36 times larger than at $400 \text{ nm} < \lambda < 450 \text{ nm}$. On the contrary, the difference in activity of CN75 under UV compared with visible light ($400 \text{ nm} < \lambda < 520 \text{ nm}$) was markedly decreased, to a factor 3.5. The low efficiency under visible light observed for both the catalysts tested was presumably due to the large recombination rate of the photogenerated electron-hole pairs, as already reported for C_3N_4 by several authors.[24] The two normalized rates for Vis-Blue and Vis-wide (last column of Table 4) were in good agreement for both the materials studied. Moreover, under visible light, the rate of CN75 was 2.7 times larger than that for C_3N_4 , and CN75 is 40% intrinsically more active than C_3N_4 . As under Vis-Blue the photon efficiency of the two materials was the same, the extended absorption of CN75 in a wider visible range made it more performing under visible light.

In addition, the kinetic order for the photodegradation of 2FP progressively shifted from pseudo-first to pseudo-zero order when moving from **UV** and **Vis-Blue** and **Vis-wide** irradiation conditions. There are two possible explanations for this change of reaction order. The first is related to the shading effect of the slurry along the light path, when a strong absorption is present. However, this was almost the same under the three irradiation conditions. Then, in the reported experiments the variation of the kinetic order can be attributed to the different density of photoactive sites that can be excited in the λ ranges considered. When all the active sites are occupied, a zero order dependence on the substrate concentration is attainable. Then, under Vis irradiation the number of sites that can be excited must be remarkably lower than under UV, or, in other words, the concentration of catalytically active intra-gap states must be lower than the charge carriers density evaluated in Table 3, column 8.

4 CONCLUSIONS

The synthesis was optimized to obtain carbon nitride with p-type semiconducting behavior, exhibiting the development of a photopotential of almost 600 mV and a larger photoactivity under visible light if compared with pristine C_3N_4 . Although the synthesis is simple and the chemicals employed are inexpensive, the new materials obtained are defective. However, even the alternative advanced synthetic routes, which allow the formation of controlled ultrathin layers with high structural order, like CVD, PVD and sputtering deposition, are not effective in replicating the 2D structure of C_3N_4 with a regular alternation of C-N aromatic bonds. We demonstrated that the exfoliation and fractioning steps are fundamental to achieve materials with the required electronic and photocatalytic features. We also determined the flat band, the valence and conduction band potentials for pristine and doped carbon nitrides, which are seldom reported, but convey valuable information. Only for large C-content (triamonopyrimidine content > 50 %) does carbon nitride display p-type doping, whereas pristine carbon

nitride is always an n-type semiconductor. This work opens up new possibilities for making heterojunctions with two organic or hybrid semiconductors, and for functionalization, given the organic nature of CN75, with metal-organic catalysts able to carry out reduction reactions of environmental interest.

ACKNOWLEDGEMENTS

The financial support from project Ricerca Locale – Torino University – and the project PHOTORECARB - Progetti di Ateneo/CSP 2012 – Call 03 – Università di Torino & Compagnia di S.Paolo - is gratefully acknowledged.

REFERENCES

- 1 V. Balzani, A. Credi, M. Venturi, Photochemical Conversion of Solar Energy, *ChemSusChem* 1 (2008) 26-58.
- 2 S. Fukuzumi, D. Hong, Y. Yamada, Bioinspired Photocatalytic Water Reduction and Oxidation with Earth-Abundant Metal Catalysts, *J. Phys. Chem. Lett.* 4 (2013) 3458-3467.
- 3 K. Kalyanasundaram, M. Graetzel, Artificial photosynthesis: biomimetic approaches to solar energy conversion and storage, *Curr. Opin. Biotechnol.* 21 (2010) 298-310.
- 4 Z. Weng, J. Jiang, Y. Wu, Z. Wu, X. Guo, K.L. Materna, W. Liu, V.S. Batista, G.W. Brudvig, H. Wang, Electrochemical CO₂ Reduction to Hydrocarbons on a Heterogeneous Molecular Cu Catalyst in Aqueous Solution, *J. Am. Chem. Soc.* 138 (2016) 8076-8079.
- 5 F. Franco, C. Cometto, L. Nencini, C. Barolo, F. Sordello, C. Minero, J. Fiedler, M. Robert, R. Gobetto, C. Nervi, Local Proton Source in Electrocatalytic CO₂ Reduction with [Mn(bpy-R)(CO)₃Br]Complexes, *Chem. Eur.J.* 23 (2017) 4782-4793.
- 6 C.W. Machan, M.D. Sampson, C.P. Kubiak, A Molecular Ruthenium Electrocatalyst for the Reduction of Carbon Dioxide to CO and Formate, *J. Am. Chem. Soc.* 137 (2015) 8564-8571.
- 7 J. Luo, L. Steier, M.K. Son, M. Schreier, M.T. Mayer, M. Grätzel, Cu₂O nanowire photocathodes for efficient and durable solar water splitting, *Nano Lett.* 16 (2016) 1848-1857.
- 8 C.C.L. McCrory, S. Jung, I.M. Ferrer, S.M. Chatman, J.C. Peters, T.F. Jaramillo, Benchmarking hydrogen evolving reaction and oxygen evolving reaction electrocatalysts for solar water splitting devices, *J. Am. Chem. Soc.* 137 (2015) 4347-4357.
- 9 S. Pitchumani, M. Vijayan, V. Krishnan, Synthesis of polythiophene n-type and p-type doping and compensation, *Bull. Electrochem.* 4 (1988) 379-381.
- 10 T. Le, Y. Kim, H. Yoon, Electrical and Electrochemical Properties of Conducting Polymers, *Polymers* 2017 (4) 150
- 11 Wen, J. Xie, X. Chen, X. Li, A review on g-C₃N₄-based photocatalysts, *Appl. Surf. Sci.* 391 (2017) 72-123
- 12 G. Mamba, A.K. Mishra, Graphitic carbon nitride (g-C₃N₄) nanocomposites: A new and exciting generation of visible light driven photocatalysts for environmental pollution remediation, *Appl. Catal. B: Environ* 198 (2016) 347–377
- 13 X. Wang, K. Maeda, A. Thomas, K. Takanabe, G. Xin, J.M. Carlsson, K. Domen, M. Antonietti, A metal-free polymeric photocatalyst for hydrogen production from water under visible light, *Nat. Mater.* 8 (2009) 76-80.
- 14 D. Masih, Y. Ma, S. Rohani, Graphitic C₃N₄ based noble-metal-free photocatalyst systems: A review, *Appl. Catal. B: Environ* 206 (2017) 556-588.
- 15 T.Y. Wang, X. Wang, M. Antonietti, Polymeric Graphitic Carbon Nitride as a Heterogeneous Organocatalyst: From Photochemistry to Multipurpose Catalysis to Sustainable Chemistry, *Angew. Chem. Int. Ed.* 51 (2012) 68-89.

-
- 16 Y. Qiu, L. Gao, P-Type Carbon Nitride Synthesized by a Gas-Solid Reaction, *J. Am. Ceram. Soc.* 87 (2004) 1598-1601.
 - 17 D. Wang, W. Gu, Y. Zhang, Y. Hu, T. Zhang, X. Tao, W. Chen, Novel C-rich carbon nitride for room temperature NO₂ gas sensors, *RSC Adv.* 4 (2014) 18003-18006.
 - 18 X. Bai, C. Sun, S. Wu, Y. Zhu, Enhancement of photocatalytic performance via a P3HT-g-C₃N₄ heterojunction, *J. Mater. Chem. A* 3 (2015) 2741-2747.
 - 19 W. Ho, Z. Zhang, W. Lin, S. Huang, X. Zhang, X. Wang, Y. Huang, Copolymerization with 2,4,6-Triaminopyrimidine for the Rolling-up the Layer Structure, Tunable Electronic Properties, and Photocatalysis of g-C₃N₄, *ACS Appl. Mater. Interfaces* 7 (2015) 5497-5505.
 - 20 G. Dong, K. Zhao, L. Zhang, Carbon self-doping induced high electronic conductivity and photoreactivity of g-C₃N₄, *Chem. Commun.*, 48 (2012), 6178-6180
 - 21 L. Jianga, X. Yuana, Y. Pana, J. Lianga, G. Zenga, Z. Wua, H. Wang, Doping of graphitic carbon nitride for photocatalysis: A review, *Appl. Catal., B* 217 (2017) 388-406.
 - 22 C. Minero, E. Pramauro, E. Pelizzetti, V. Degiorgio, M. Corti, Micellar properties of sodium dodecylpoly(oxyethylene) sulfates, *J. Phys. Chem.* 90 (1986) 1620-1625.
 - 23 J. Liu, T. Zhang, Z. Wang, G. Dawson, W. Chen, Simple pyrolysis of urea into graphitic carbon nitride with recyclable adsorption and photocatalytic activity, *J. Mater. Chem.* 21 (2011) 14398-14401.
 - 24 A. Thomas, A. Fischer, F. Goettmann, M. Antonietti, J.O. Muller, R. Schlogl, J.M. Carlsson, Graphitic carbon nitride materials: variation of structure and morphology and their use as metal-free catalysts, *J. Mater. Chem.* 18 (2008) 4893-4908.
 - 25 V. Štengl, J. Henych, M. Slušná, P. Ecorchard, Ultrasound exfoliation of inorganic analogues of graphene, *Nanoscale Res. Lett.* 9 (2014) 167.
 - 26 P. Sharma, Y. Sasson, Highly active g-C₃N₄ as a solid base catalyst for Knoevenagel condensation reaction under phase transfer conditions, *RSC Adv.* 2017 (7) 25589
 - 27 G. Chen, W. Weng, D. Wu, C. Wu, J. Lu, P. Wang, X. Chen, Preparation and characterization of graphite nanosheets from ultrasonic powdering technique, *Carbon* 42 (2004) 753-759.
 - 28 F.T. Johra, J. Lee, W. Jung, Facile and safe graphene preparation on solution based platform, *J. Ind. Eng. Chem.* 20 (2014) 2883-2887
 - 29 T. Komatsu, The First Synthesis and Characterization of Cyameluric High Polymers, *Macromol. Chem. Phys.* 202 (2001) 19-25.
 - 30 J. Tauc, Optical properties of amorphous semiconductors, in J. Tauc (Ed.), *Amorphous and Liquid Semiconductor*, Plenum Publ. Co, New York, 1974, p. 159-220.
 - 31 S. Ebraheem, A. El-Saied, Band Gap Determination from Diffuse Reflectance Measurements of Irradiated Lead Borate Glass System Doped with TiO₂ by Using Diffuse Reflectance Technique, *Mater. Sci. Appl.* 4 (2013) 324-329.
 - 32 J. Torrent, V. Barrón, Diffuse Reflectance Spectroscopy, in A.L. Ulery, L.R. Drees (Eds.) *Methods of Soil Analysis. Part 5. Mineralogical Methods*, Soil Science Society of America Inc., Madison, Wisconsin (2008) 367-386, ISBN: 978-0-89118-846-9.
 - 33 V. Kumar, S.K. Sharma, T.P. Sharma, V. Singh, Band gap determination in thick films from reflectance measurements, *Opt. Mater.* 12 (1999) 115-119.
 - 34 D. Monllor-Satoca, R. Gomez, Electrochemical Method for Studying the Kinetics of Electron Recombination and Transfer Reactions in Heterogeneous Photocatalysis: The Effect of Fluorination on TiO₂ Nanoporous Layers, *J. Phys. Chem. C* 112 (2008) 139-147.
 - 35 P. Chuang, K. Wu, T. Yeh, H. Teng, Extending the p-Conjugation of g-C₃N₄ by Incorporating Aromatic Carbon for Photocatalytic H₂ Evolution from Aqueous Solution, *ACS Sustainable Chem. Eng.* 4 (2016) 5989-5997
 - 36 C. Minero, C. Aliberti, E. Pelizzetti, R. Terzian, N. Serpone, Kinetic Studies in Heterogeneous Photocatalysis. 6. AM1 Simulated Sunlight Photodegradation over Titania in Aqueous Media: A First Case of Fluorinated Aromatics and Identification of Intermediates, *Langmuir* 7 (1991) 928-936.
 - 37 C. Minero, D. Vione, A quantitative evaluation of the photocatalytic performance of TiO₂ slurries, *Appl. Catal. B Environ.* 67 (2006) 257-269.

-
- 38 G. Camera-Roda, V. Augugliaro, A.G. Cardillo, F. Parrino, F. Santarelli, A reaction engineering approach to kinetic analysis of photocatalytic reactions in slurry systems, *Catal. Today* 259 (2016) 87-96.